PHOTONICS Research

High-order multilayer-coated blazed grating for a high-transmission and high-resolution tender X-ray monochromator/spectrometer

Yeqi Zhuang,[1] Qiushi Huang,[1,*] Andrey Sokolov,[2,4] Stephanie Lemke,[2] Zhengkun Liu,[3] Yue Yu,[1] Igor V. Kozhevnikov,[1] Runze Qi,[1] Zhe Zhang,[1] Zhong Zhang,[1] Jens Viefhaus,[2] and Zhanshan Wang[1,5]

[1]Key Laboratory of Advanced Micro-Structured Materials MOE, Institute of Precision Optical Engineering, School of Physics Science and Engineering, Tongji University, Shanghai 200092, China
[2]Helmholtz-Zentrum Berlin für Materialien und Energie, BESSY-II, 12489 Berlin, Germany
[3]National Synchrotron Radiation Laboratory, University of Science and Technology of China, Hefei 230029, China
[4]e-mail: andrey.sokolov@helmholtz-berlin.de
[5]e-mail: wangzs@tongji.edu.cn
*Corresponding author: huangqs@tongji.edu.cn

Received 11 April 2024; revised 5 November 2024; accepted 18 November 2024; posted 18 November 2024 (Doc. ID 523591); published 17 January 2025

Grating optics lie in the heart of X-ray spectroscopy instruments. The low efficiency and angular dispersion of conventional single-layer-coated gratings significantly limit the transmission and energy resolution of monochromators and spectrometers, particularly in the tender X-ray region (E = 1–5 keV). Multilayer-coated blazed gratings (MLBGs) operating at high diffraction orders offer the advantage of achieving both high efficiency and high dispersion simultaneously. Tender X-ray monochromators and spectrometers using different high-order MLBGs have been designed, all demonstrating one to two orders of magnitude higher transmission compared to conventional systems. By employing a 2400 l/mm MLBG at the −4th or −8th diffraction order, the theoretical energy resolution of the instrument is improved by two to three times at 2.5 keV. Two MLBGs operating at the −2nd and −4th orders have been fabricated, showcasing remarkable efficiencies of 34%–12% at 2.5 keV, surpassing that of single-layer-coated gratings by an order of magnitude. Further optimization of manufacturing accuracy can yield even higher efficiencies. The measured angular dispersion agrees well with theoretical predictions, supporting the potential for high resolution. High-order MLBG optics pave the way for a new generation of tender X-ray monochromators/spectrometers that offer both high transmission and high resolution. © 2025 Chinese Laser Press

https://doi.org/10.1364/PRJ.523591

1. INTRODUCTION

X-ray spectroscopy serves as a unique tool for probing the atomic and electronic structures of materials [1–6]. When combined with the advanced light sources like synchrotron radiation facilities and free electron lasers, it can unravel the information from the number and types of atoms and their interatomic structure to elementary excitations like charge-transfer, and magnetic and orbital degrees of freedom, which cannot be observed otherwise [7–17]. Photon flux and energy resolution are the two fundamental criteria that determine the capability of an X-ray spectroscopy instrument. These criteria are primarily affected by the dispersion performance of optics in the monochromator and spectrometer. Gratings are the main dispersion optics in the soft and tender X-ray regions [18]. Conventional single-layer-coated gratings have relatively low efficiency, particularly in the tender X-ray region. As the efficiency decreases with higher line density and higher orders, the energy resolution is also limited. For example, the −1st order efficiency of a 2400 l/mm blazed grating with Au coating is less than 3% in the tender X-ray region [19]. Moreover, achieving high resolution in beamlines or spectrometers requires long diffraction arms, often tens of meters, which leads to increased instrument size and higher costs [20–25]. The poor performance of the gratings also limits further improvements of X-ray spectroscopy resolution.

Combining multilayer coatings with gratings dramatically increases the diffraction efficiency, based on the quasi-Bragg diffraction effect [26–29]. Voronov *et al.* fabricated a Mo/Si-coated blazed grating that achieved a first order efficiency of 58% at 13.3 nm [30]. Ohresser *et al.* fabricated a

Mo_2C/B_4C-coated laminar grating that operates at the −1st order, exhibiting an experimental efficiency of nearly 27% at 2.2 keV [27]. Following these advancements, multilayer-coated laminar gratings for tender X-rays were implemented in the LUCIA and DEMIOS beamlines at the SOLEIL synchrotron radiation facility [31,32]. Sokolov and Huang *et al.* further enhanced this technology by designing and fabricating a Cr/C-coated blazed grating, reaching −1st order efficiencies of 45% at 2.2 keV and 60% at 3.0 keV. The latter one is approximately 40 times higher than that of single-layer-coated gratings [19]. Based on their findings, a high-efficiency multilayer-coated blazed grating (MLBG) was developed and installed in the monochromator of U41-PGM1 beamline at the BESSY II synchrotron radiation facility. This implementation resulted in a two-orders-of-magnitude increase in photon flux found around 2.5 keV, significantly improving the imaging and spectroscopic capabilities of the beamline [33]. However, compared to single-layer-coated gratings, multilayer gratings require a larger grazing incidence angle to satisfy the quasi-Bragg condition. As a result, a multilayer grating operating at the −1st diffraction order exhibits reduced angular dispersion and relatively low energy resolution.

High diffraction orders significantly improve the angular dispersion of a grating, which is particularly advantageous for MLBGs, as they maintain high efficiency even when operating at high orders. Voronov *et al.* proposed using high-order multilayer gratings in a soft X-ray spectrometer [34]. A W/B_4C-coated blazed grating was fabricated, showing a diffraction efficiency of 14% at 700 eV in the second order [35]. Nevertheless, the potential of high-order MLBGs, when combined with monochromators and spectrometers for increased transmission and resolution, has not been extensively studied especially in the tender X-ray region. The performance of high-order MLBGs also requires further experimental demonstration and analysis.

In this paper, tender X-ray monochromators and spectrometers using MLBGs operating in high diffraction orders were designed and compared for the first time. The implementation of high-order MLBGs significantly increases the theoretical instrument transmission by orders of magnitude and enhances energy resolution by several folds. In addition, high-order MLBGs allow for a reduction in instrument length while maintaining state-of-the-art energy resolution. Based on the conducted analysis, two high-order MLBG samples were developed, showing high diffraction efficiency and angular dispersion consistent with theoretical predictions. The impact of MLBG structure imperfections on high-order efficiency was also analyzed, providing guidance for future improvement.

2. DESIGN

A. Design of MLBGs

Figure 1(a) shows the schematic of an MLBG structure. To achieve high efficiency at higher diffraction orders, MLBGs are required to be operated in the single-order regime, i.e., only one diffraction order is effectively amplified. The incident/diffracted beams need to satisfy the grating equation and the quasi-Bragg reflection conditions simultaneously [27,28].

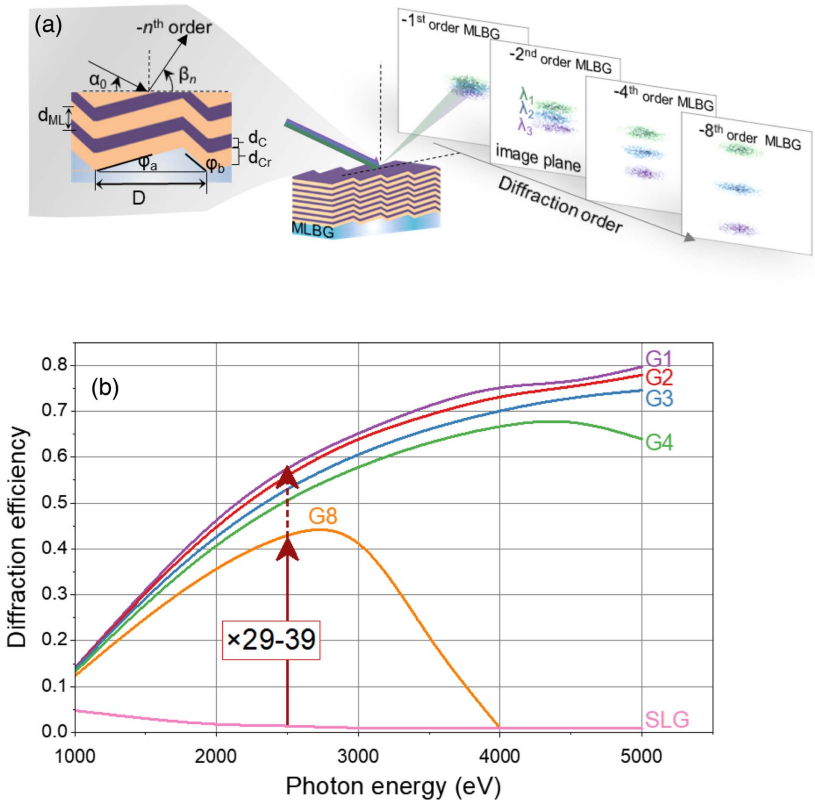

Fig. 1. (a) Schematic of the MLBG structure and illustration of improved energy resolution with high-order MLBGs. (b) Theoretical diffraction efficiency of MLBGs (G1, G2, G3, G4, and G8), compared to Rh-coated grating (SLG).

Higher diffraction orders, which result in greater asymmetric diffraction, affect diffraction efficiency, but the drop can be minimized by optimizing both the grating and multilayer structures. Meanwhile, higher diffraction orders bring much stronger angular dispersion, defined by the equation $|n| \cdot a_0 / \cos \beta_n$ (where n is the diffraction order, a_0 is the grating line density, and β_n is the diffraction angle), leading to significantly improved energy resolution.

For illustration, five MLBGs were optimized at 2.5 keV across different diffraction orders, including the −1st, − 2nd, −3rd, − 4th, and −8th orders. The −8th order is the highest diffraction order analyzed here, as the multilayer d-spacing gradually decreases with increasing order. The 3 nm multilayer d-spacing required for the −8th order represents the minimum achievable with good quality using current technology. The structural parameters of these MLBGs are listed in Table 1. The diffraction efficiency in the 1–5 keV range was calculated using the DiffractMOD software [36], as shown in Fig. 1(b). The diffraction efficiency of higher orders is comparable to that of the −1st order when grazing incidence angle is essentially larger than the total external reflection (TER) region. For example, at 2.5 keV, the diffraction efficiencies are 58% for the −1st order, 56% for the −2nd, 51% for the −4th, and 44% for the −8th. These values are around 29–39 times higher than those of the single-layer-coated grating (2400 l/mm). For higher orders, the grazing incidence angle approaches the TER region at lower energies, resulting in a decline in high-order efficiency. This phenomenon occurs due to the progressively increased blaze angles and smaller multilayer d-spacings required for higher orders. Consequently, the working energy range is reduced at high orders, particularly for the −8th order. However, even for the −8th order, a theoretical efficiency above 20% is maintained at 3.5 keV. The efficiency at selected energies can be further optimized by tailoring the MLBG structure to balance with the required resolution.

Based on the designed MLBGs, the effects of high diffraction orders are examined in the context of commonly used tender X-ray instruments for high resolution, such as the collimated plane grating monochromator (cPGM) and spherical variable-line-spaced (SVLS) grating spectrometer [20,21,37]. For more details, refer to Appendix A for cPGM and Appendix B for the spectrometer. The following discussion also includes the instruments that use single-layer-coated optics for comparison. In this instance, the single-layer-coated grating has the same line density of 2400 l/mm to achieve high resolution, with its coating material, blaze angle, and incidence angle optimized for high efficiency.

B. MLBG-Based Ultrahigh-Resolution Design: Photon Transmission Performance

A cPGM is designed to keep parallelism between the entrance and exit light throughout the scanning in the whole operating energy range by simultaneously adjusting two optics: the mirror and the grating, as shown in Fig. 2(a). The monochromator transmission was evaluated by the product of the mirror's reflectance and the grating's efficiency. In Fig. 2(c), the transmission of a conventional cPGM with Rh-coated optics is very low, showing only 0.17% at 2.5 keV (11% from the mirror × 1.5% from the grating). The poor transmission results from both the inherently low diffraction efficiency of a single-layer-coated grating with high line density, as well as the reduced reflectivity of the mirror. The mirror is expected to be operated outside the high-reflectivity region to fulfill the parallelism requirement. A similar low transmission of a monochromator with a high line density grating was observed at 2.0 keV [38]. However, by applying multilayer coatings on both optics, the monochromator transmission increases to 36%, even when using the −4th order (70% from the mirror × 51% from the grating) at 2.5 keV, corresponding to a 320-fold enhancement.

In the spectrometer, scattered radiation from the sample is collected and dispersed onto the detector using an SVLS grating, as shown in Fig. 2(b). The spectrometer's transmission is determined by the diffraction efficiency of the grating and the ratio of the grating's collection solid angle to 4π. To calculate the solid angle, the illuminated area on the grating is set to 160 mm (length) × 20 mm (width) for all MLBGs. Figure 2(d) shows that the design with the Rh-coated grating exhibits a low spectrometer transmission of approximately 2.7×10^{-8} at 2.5 keV. This low transmission comes from the low-diffraction efficiency and small grazing incidence angle on the grating, which limits the collection solid angle. MLBGs operating under the Bragg diffraction condition provide both high efficiency and a large operating angle, resulting in much higher spectrometer transmission [39]. The transmission of the MLBG-based design using different high orders is 7.4×10^{-7} to 1.0×10^{-6} at 2.5 keV, which is 27–37 times higher than that of the single-layer-coated grating design. These results demonstrate that high-diffraction-order MLBGs significantly increase the theoretical transmission of cPGMs and spectrometers by 27–320 times. Such improvements are crucial for photon-hungry techniques like RIXS.

C. MLBG-Based Ultrahigh-Resolution Design: Energy Resolution Performance

The energy resolution of a cPGM beamline or spectrometer was calculated analytically, considering components such as

Table 1. Structural Parameters and Grazing Incidence Angle at 2.5 keV for MLBGs at Various Diffraction Orders

Grating Number	Operation Order	Grating Line Density (l/mm)	Blaze Angle (deg)	Anti-blaze Angle (deg)	Multilayer Material	γ_{Cr}	d-Spacing (nm)	Period Number	Grazing Incidence Angle (deg)
G1	−1st	2400	0.90	2.10	Cr/C	0.4	5.38	100	2.10
G2	−2nd	2400	1.20	2.80	Cr/C	0.4	4.08	100	2.52
G3	−3rd	2400	1.50	3.50	Cr/C	0.4	3.50	100	2.77
G4	−4th	2400	1.90	4.43	Cr/C	0.4	3.36	100	2.55
G8	−8th	2400	3.31	7.48	Cr/C	0.4	3.00	100	1.70

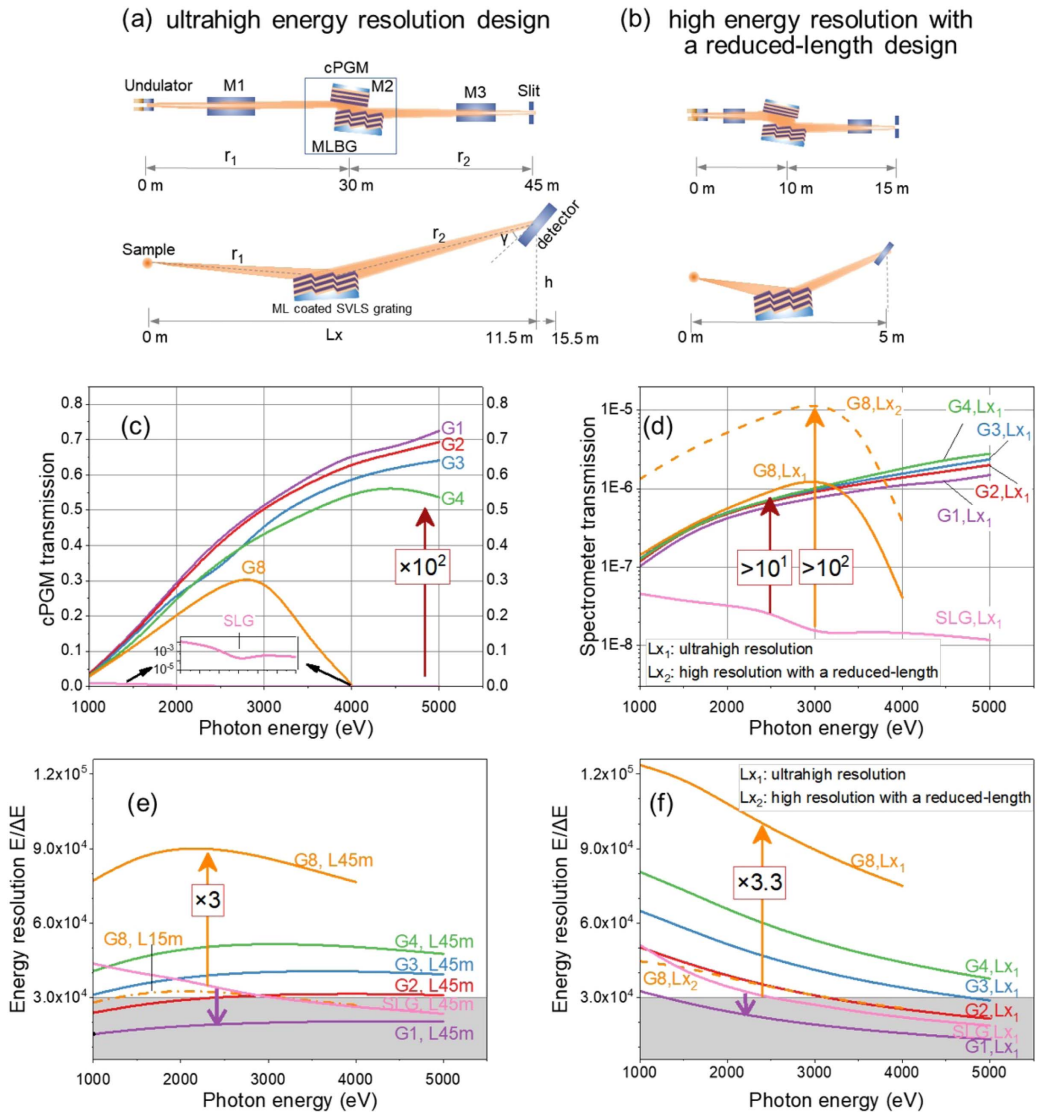

Fig. 2. (a) Schematic of the ultrahigh-resolution design of the cPGM beamline and the SVLSG spectrometer using MLBG. (b) Schematic of high-resolution design of cPGM beamline and spectrometer with reduced instrument length. (c) Theoretical diffraction efficiency of gratings and transmission of the cPGM. (d) Transmission of the spectrometer. (e), (f) Energy resolution of the beamlines/spectrometer with the grating operating in different diffraction orders. Lx_1 and Lx_2 represent the lengths of the SVLSG spectrometer for high energy resolution and reduced-length design, respectively. M1, collimated mirror; M2, plane mirror; M3, focus mirror; MLBG, multilayer-coated blazed grating; r_1, entrance arm length; r_2, exit arm length; Lx, total spectrometer length; h, focal height; y, inclination angle of detector.

the source, mirror, and exit slit/detector [20,37] (see equations in Appendices A and B).

As shown in Fig. 2(e), the cPGM beamline using the −1st diffraction order achieves an energy resolution of 3.2×10^4 with Rh-coated optics and 1.1×10^4 with multilayer-coated optics at 2.5 keV. The relatively low energy resolution of the beamline with the −1st order MLBG is primarily due to the large grazing incidence angle of the MLBG, which leads to a small angular dispersion between two adjacent energies. Moreover, the large grazing incidence angle reduces the number of effectively illuminated grating grooves, broadening the angular bandwidth of the diffraction efficiency curve and further decreasing energy resolution. However, these effects can be well mitigated by operating the MLBG at higher diffraction orders. For example, the energy resolution of the cPGM using the −2nd diffraction order MLBG reaches 3.0×10^4, approaching that of the Rh-coated grating system. As the diffraction order increases, energy resolution continues to improve. At the −3rd diffraction order, the energy resolution is 3.9×10^4, and at the −4th diffraction order, it reaches 5.1×10^4 – 1.6 times higher than that achieved with the Rh-coated grating. Operating the MLBG in the −8th diffraction order brings an ultrahigh energy resolution of 9.0×10^4, approximately three times higher than that of a single-layer-coated grating system.

For SVLS grating spectrometers, the additional structural parameters of an SVLS grating, including the curvature radius and higher-order VLS coefficients, are individually optimized for different diffraction orders at 2.5 keV. The optimization

is based on the grating equation and the coma cancellation condition. The spectrometer geometry is configured for variable-energy operation with a fixed detector inclination angle. This design takes into account the mechanical constraints typical for RIXS spectrometers [20,37]. Detailed structural parameters of the SVLS grating and the spectrometer geometry are listed in Table 3 in Appendix B, with corresponding resolutions shown in Fig. 2(f). The spectrometer with an Rh-coated grating achieves an energy resolution of 3.0×10^4 at 2.5 keV, while the spectrometer using the −1st order MLBG has an energy resolution of 2.1×10^4, due to similar limitations observed in the cPGM beamline. As the diffraction order increases, the energy resolution continues to improve. The spectrometer with the −2nd order achieves an energy resolution of 3.4×10^4, while the −4th order MLBG reaches 5.9×10^4, which is twice as high as that of the Rh-coated grating. Operating the MLBG in the −8th diffraction order further enhances energy resolution to an ultrahigh value of 9.8×10^4, approximately 3.3 times higher than that with a single-layer-coated grating.

These simulation results show that both the cPGM beamline and the SVLS grating spectrometer, using high-order MLBGs, simultaneously provide orders of magnitude higher transmission and several times higher energy resolution, compared to the conventional single-layer-coated grating.

D. MLBG-Based High Resolution with a Reduced-Length Design

The ultrahigh energy resolution offered by the high-order MLBGs also enables shorter beamlines and spectrometers while maintaining a resolution comparable to that of current setups. For example, a 15-m-long cPGM beamline using the −8th diffraction order MLBG achieves a theoretical resolution of 3.2×10^4 at 2.5 keV, which is close to the resolution of a 45-m-long cPGM beamline that employs a −1st order single-layer-coated grating. Moreover, despite the reduced size, the transmission of the 15-m-long cPGM beamline is still two orders of magnitude higher than that of the conventional design. Similarly, for the case of reducing the spectrometer length from ∼15 m to 5 m, the −8th order MLBG still enables an energy resolution of 3.4×10^4 at 2.5 keV. Notably, the shorter distance between the sample and the SVLS grating increases the collection solid angle, further enhancing the transmission up to 8.8×10^{-6}. This transmission exceeds that of previously discussed ultrahigh-resolution spectrometer designs and is two orders of magnitude greater than that of conventional setups. Shorter spectrometer length also permits the positioning of multiple spectrometers around the sample, facilitating the simultaneous collection of emission signals from different wavelength bands or elements, as well as other new functions. This greatly enhances the capability of the spectrometer.

3. FABRICATION AND CHARACTERIZATION OF HIGH-DIFFRACTION-ORDER MLBGS

To showcase the performance of high-order MLBGs, two MLBGs were designed and fabricated. The first MLBG, S1, was designed to operate in the −2nd diffraction order at 2.5 keV. Its grating substrate, fabricated at the Precision Gratings Department at Helmholtz-Zentrum Berlin by mechanical ruling [18], has a groove density of 2400 l/mm, a blaze angle of 1.3°, and an anti-blaze angle of 3.0°. The target multilayer *d*-spacing of S1 is 4.0 nm, with a Cr thickness to *d*-spacing ratio of 0.45. The second MLBG, S2, was designed to fulfill the resonant condition of the −4th diffraction order at 2.5 keV. Its grating substrate, produced at the Grating Department of the National Synchrotron Radiation Laboratory in China using wet etching, features a larger blaze angle of 1.93° and an anti-blaze angle of 7.38°. The grating line density of S2 is the same as that of S1, and its multilayer *d*-spacing is 3.9 nm. Both samples consist of 60 bilayers of multilayer structures [19]. The multilayer deposition was carried out using direct current magnetron sputtering technology. The base pressure in the deposition chamber was 3.0×10^{-4} Pa, with high purity Ar as the working gas. The deposition rates were 0.027 nm/s for C and 0.12 nm/s for Cr. These two MLBGs were designed based on the available blazed gratings, especially the blaze angle. Their performance would improve if the desired blaze angle could be manufactured.

The internal multilayer structures of S1 and S2 were characterized using transmission electron microscopy (TEM), as illustrated in Figs. 3(a) and 3(c). The surface profiles of the gratings were measured using atomic force microscopy (AFM) before and after multilayer deposition, as shown in Figs. 3(b) and 3(d). Both TEM images and AFM images show that the grating groove profile is well replicated during multilayer deposition. Meanwhile, the grating substrate profiles of both samples deviate from an ideal triangle shape. The primary imperfection of the groove profile of S1 is the rounded apexes of the triangular grooves, while the main imperfection of S2 is the non-flatness of the blazed facets. These profile imperfections cause a variation in the local blazed facets and result in a mismatch of the resonant condition between the multilayer and the grating. Additionally, the surface roughness differs between the two substrates, measuring 0.25 nm (RMS) for S1 and 0.51 nm for S2. The multilayer interfaces of S1 are also sharper than that of S2, as observed in Figs. 3(a) and 3(c). The impact of these structural imperfections on diffraction efficiency will be further discussed in Fig. 3.

The optical performance of the fabricated MLBGs and the witness multilayers on flat wafers was measured in the tender X-ray range. These measurements were performed at the optics beamline PM-1 for the energy range of 0.7–1.8 keV and the KMC-1 beamline for the energy range of 2.1–6 keV, both situated in the BESSY-II synchrotron radiation facility.

The measured reflectance of the witness multilayer for S1 and the diffraction efficiency of S1 and S2, plotted as a function of photon energy, are presented in Figs. 4(a) and 4(b). These experimental results were compared with the theoretical predictions for both an ideal multilayer and MLBGs.

For S1, the measured reflectance of the witness sample follows the predicted trend, which gradually increases with energy and peaks at 4–5 keV. At 2.5 keV, the reflectance is 50%, representing 75% of its theoretical value. The measured diffraction efficiency of the −2nd order similarly shows an increasing trend as predicted, reaching 34% at 2.5 keV and over 50% at 4–5 keV. The experimental −2nd order efficiency is

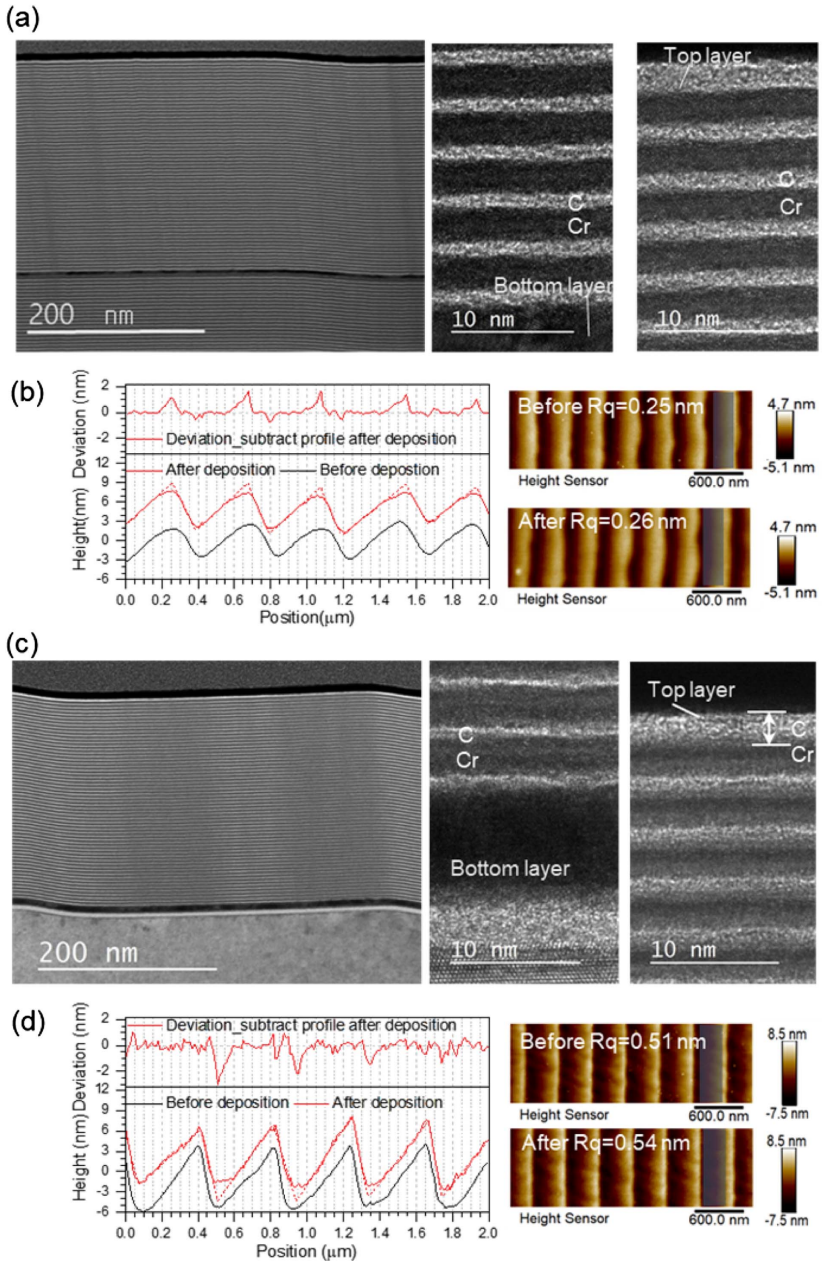

Fig. 3. Characterization of the fabricated MLBG structures. Cross-sectional TEM images of S1 (a) and of S2 (c) reveal the detailed internal structures. The additional dark stripes in the TEM image of sample S1 are due to it being a recoated sample. AFM images and the corresponding extracted 1D profiles of S1 (b) and S2 (d) are presented, along with deviation curves that illustrate the differences between the measured profiles (solid line) and the ideal triangle profiles (dashed line).

approximately 75% of the theoretical value (relative efficiency), indicating that the slight decrease in efficiency compared to theory is mainly due to the quality of the multilayer deposited on the grating. The measured −3rd order efficiency is 17% at 2.5 keV and 24% at 4 keV, corresponding to about 57% of the theoretical efficiency. This lower relative efficiency compared to the −2nd order suggests that the higher-order diffraction efficiency is more sensitive to structural deviations and imperfections.

For S2, the measured curves also follow a similar trend to the theoretical predictions. Considering the larger roughness of 0.5 nm [Fig. 3(d)], the estimated reflectance of the deposited multilayer is around 67% of the theoretical value. The measured −3rd order diffraction efficiency is 12% at 2.5 keV and close to 20% at 4–5 keV. The measured −4th order efficiency is 15% at 2.5 keV. The relative efficiency of both the −3rd and −4th orders is approximately 35%. The larger discrepancy between the experimental and theoretical efficiency of S2 compared to S1 can be caused by the more severe structural imperfections of the S2 grating. Nevertheless, the −3rd and −4th order efficiencies of S2 are still 10–20 times higher than the −1st order efficiency of an Rh-coated grating with the same

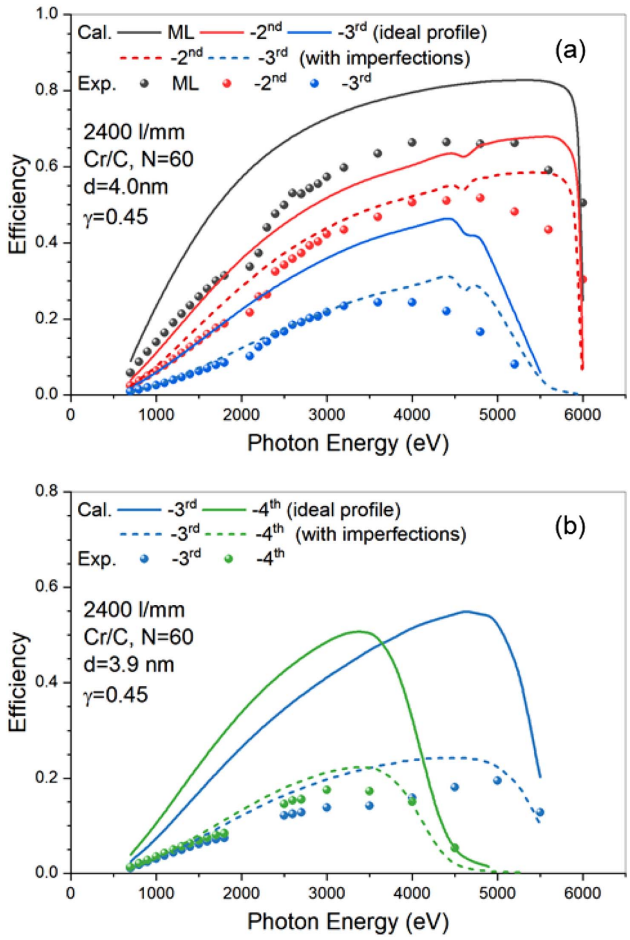

Fig. 4. (a) The experimental and theoretical reflectance of the first order of the reference multilayer (black spheres and black lines). The experimental (spheres) and theoretical diffraction efficiency with and without imperfections (dashed and solid lines) of the −2nd diffraction order (red) and the −3rd order (blue) of the MLBG S1. (b) The experimental (spheres) and theoretical diffraction efficiency with and without imperfections (dashed and solid lines) of the −3rd diffraction order (blue) and the −4th diffraction order (green) of the MLBG S2.

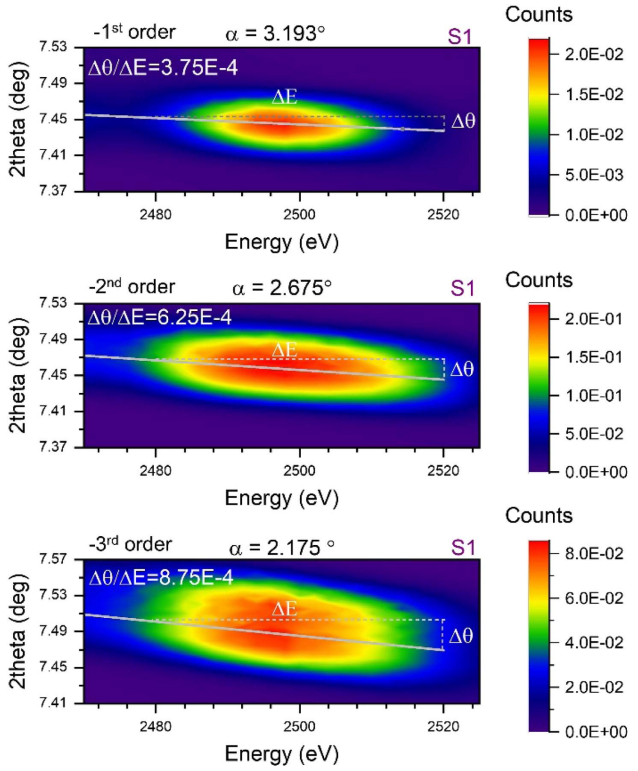

Fig. 5. Two-dimensional diffraction measurements as a function of detector angle and photon energy of the S1 at a grazing incidence angle of 3.193° in the −1st diffraction order, 2.675° in the −2nd order, and 2.175° in the −3rd order.

line density in the tender X-ray range. The effect of structural imperfections on high-order efficiency is discussed in the next section.

To evaluate the angular dispersion of the optics, two-dimensional scans of both photon energy and diffraction angle for S1 were performed under fixed incidence. The dispersion was measured at the resonant conditions of S1 of the −1st, −2nd, and −3rd orders. As shown in Fig. 5, the central high-efficiency area is attributed to the satisfaction of the resonant condition. The slope of the variation of the diffraction angle versus energy ($\Delta\theta/\Delta E$) represents the angular dispersion of the grating. The experimental angular dispersion is 3.75×10^{-4} deg/eV of the −1st order, 6.25×10^{-4} deg/eV of the −2nd order, and 8.75×10^{-4} deg/eV of the −3rd order. The angular dispersion increases with higher diffraction orders, consistent with the predictions of the grating equation. The angular dispersion of the −3rd order of S1 is 1.7 times larger than that of the −1st order of an Rh-coated grating with the same line density. The two-dimensional map also shows that the angular width (full-width at half-maximum, FWHM) of the diffraction peak increases with the diffraction order at a fixed photon energy. This increase occurs due to the stronger expansion effect inherent in the high-order diffraction geometry, which enlarges the beam size. In beamline applications, the beam size broadening can be eliminated using a focusing mirror, while the much larger angular dispersion enhances energy resolution.

4. ANALYSIS OF STRUCTURAL IMPERFECTIONS ON THE PERFORMANCE OF HIGH-ORDER MLBGS

To analyze the efficiency drop in higher diffraction orders, six typical structural imperfections were identified and their individual effects on efficiency were examined in the context of the MLBGs listed in Table 1, where the structure is optimized to maximize the efficiency of a specific order. The typical structural imperfections include the multilayer interface width, the rounded apexes of the grating groove profile, the lateral uniformity of the multilayer *d*-spacing, the uniformity of the blaze and anti-blaze angles, and the grating period. Three methods were used to simulate the structural imperfections. For the multilayer interface width, which is difficult to integrate directly into the MLBG model, its effect on MLBG efficiency was evaluated by calculating the ratio of multilayer reflectance with

and without accounting for interface width, calculated using the IMD software [40]. The roughness was assumed to be delta-correlated [41]. The rounded apexes of the grating groove profile were directly incorporated into the grating groove profile in the DiffractMOD simulation. For the remaining imperfections, three typical values—namely, the design value and the left and right boundaries of the defect fluctuation range—were separately input into the MLBG model to simulate efficiency. The resulting efficiencies were then averaged and normalized to the design value. The simulation results, along with the schematic of structural imperfections, are shown in Fig. 6. In addition, the individual effects of primary imperfections of S1 and S2 on their efficiency were also discussed.

Four out of six structural imperfections significantly affect grating efficiency, with the impact becoming more pronounced at higher diffraction orders. These critical imperfections include the multilayer interface width, the rounded apexes of the grating groove profile, the uniformity of the blaze angle, and the lateral uniformity of multilayer *d*-spacing. With a multilayer interface width of 0.4 nm, the relative efficiencies of the MLBG decrease from 95% for the −1st diffraction order to 89% for the −2nd, 84% for the −3rd, and 82% for the −4th. The decrease in relative efficiency might be attributed to the increasing influence of interface width as the multilayer *d*-spacing decreases, which is typically required for higher diffraction orders [27]. Moreover, a larger interface width generally leads to lower efficiency across all orders, partially explaining the lower efficiency of S2 compared to S1. The rounded apexes of the grating groove profile are simplified as a triangle shape in the analysis. The triangle's width is 25% of the grating period, with an angle corresponding to 65% of the blaze angle, according to AFM images of S1. Under these conditions, the structures designed for specific orders have relative efficiencies of around 100% for the −1st order, 98% for the −2nd, 95% for the −3rd, and 94% for the −4th. Due to the different grating fabrication technologies, the main structural imperfection of S2 is the non-flatness of the blazed facets, resulting in a variation of the blaze angle of around ±18%. This variation leads to relative efficiencies of 99% for the −1st order, 94% for the −2nd, 86% for the −3rd, and 73% for the −4th. The lateral uniformity of the multilayer *d*-spacing at 1% results in a similar efficiency loss for higher orders. These decreases in relative efficiency indicate that higher-order efficiency has less tolerance for the structural mismatches between the multilayer and grating [27]. The other two imperfections, namely, the uniformity of the anti-blaze angle at ±50% and the grating period at 1%, have a negligible effect on relative efficiency across different orders, as shown in Fig. 6.

To evaluate the overall impact of the main imperfections in the sample on the measured diffraction efficiency, the individual effects of these imperfections were multiplied and combined with the designed efficiency. For sample S1, two imperfections were considered: the impacts of the rounded apexes were analyzed, where the blaze angle is reduced to 65% of its original value and the length of the rounded area is 25% of the grating period; the multilayer interface width, measuring 0.43 nm for both interfaces, was also included in the analysis. For sample S2, three imperfections were taken into account: the multilayer interface width (0.66 nm for the Cr-on-C interface and 0.60 nm for the C-on-Cr interface), a variation of ±18% in the blaze angle, and a lateral uniformity in multilayer *d*-spacing of 0.8%. The calculated results are illustrated by the dashed lines in Fig. 4(a) for S1 and Fig. 4(b) for S2. Incorporating these main imperfections brought the predicted efficiencies much closer to the measured results. Note that the −3rd order efficiency of S1 is significantly affected by the rounded apexes, as S1 was optimized for the −2nd order

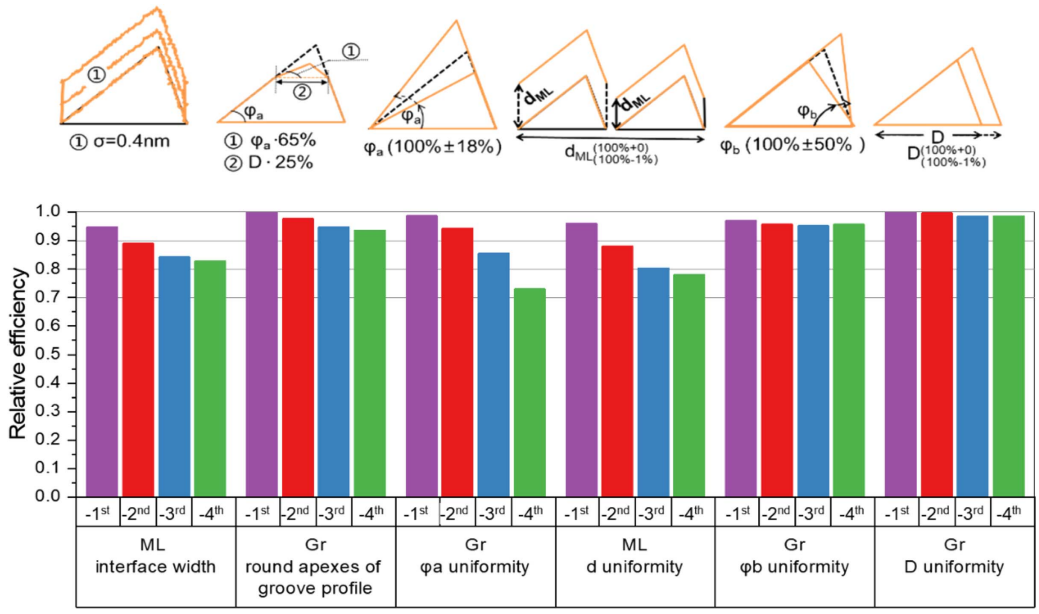

Fig. 6. Efficiency loss due to structural imperfections. The schematic of various structural imperfections is shown on the top. The efficiency loss caused by each structural imperfection was calculated at 2.5 keV and normalized against the efficiency of the ideal structure. The blaze angle and *d*-spacing were optimized to the maximum efficiency for each diffraction order, as detailed in Table 1.

efficiency, leading to a deviation from the resonant condition of the −3rd order. Consequently, higher fabrication accuracy in the first four structural parameters is essential to improve the diffraction efficiency of high-order MLBGs.

5. CONCLUSION AND OUTLOOK

High-diffraction-order MLBGs with both high efficiency and resolution in the tender X-ray region were designed and experimentally demonstrated. Simulations of representative cPGM beamlines and SVLSG spectrometers using high-order MLBGs showed that the transmission of both systems is increased by one to two orders of magnitude compared to the case with a conventional single-layer-coated grating, given to the dramatically improved diffraction efficiency and collection solid angle. The energy resolution of the beamline and spectrometer gradually increases with diffraction order, reaching an ultrahigh value of $\sim 9.0 \times 10^4$ in the eighth diffraction order, which is around three times higher than that of a single-layer-coated grating. High-order MLBGs also enable a shorter instrument design, achieving much higher transmission while maintaining a resolution comparable to that of currently high-resolution setups.

Two MLBGs operating in the −2nd, −3rd, and −4th diffraction orders were fabricated and characterized. The experimental efficiencies are 34%–12% at 2.5 keV, which is 22–8 times higher than that of the Rh-coated grating. The experimental efficiencies of higher orders show larger discrepancies from the theoretical values, primarily due to the fabrication imperfections in the MLBG structure. Some of these imperfections have a more pronounced effect on higher diffraction orders. The experimental angular dispersion is in good agreement with the theoretical prediction, with the −3rd diffraction order dispersion of sample S1 being 1.7 times larger than that of the Rh-coated grating with the same line density. The experimental results confirm that high-order MLBGs have great potential to improve the energy resolution by several times and the total transmission by orders of magnitude for both monochromators and spectrometers in the tender X-ray energy range. The experimental performance of high-order MLBGs can be further enhanced by improving manufacturing accuracy. This work contributes towards the realization of a new generation of high-transmission and high-resolution tender X-ray spectroscopic instruments.

APPENDIX A: ENERGY RESOLUTION OF THE BEAMLINE

The beamline energy resolution is considered as the sum of the following six individual contributions, namely, the photon source, the collimated mirror, the plane mirror, the grating, the focus mirror, and the exit slit [20,42,43]:

$$\Delta E_S = 2.35 \cdot \sqrt{\frac{\lambda L}{2\pi^2} + \Sigma_y^2} \cdot \frac{\sin\alpha}{r_1 a_0 |n| \lambda} E, \tag{A1a}$$

$$\Delta E_{\mathrm{CM}} = 2.35 \cdot (2\delta_{\mathrm{CMs}}) \cdot \frac{\sin\alpha_0 \cdot \sin\theta_{\mathrm{CM}}}{a_0 |n| \lambda} E, \tag{A1b}$$

$$\Delta E_{\mathrm{PM}} = 2.35 \cdot (2\delta_{\mathrm{PMt}}) \cdot \frac{\sin\alpha_0}{a_0 |n| \lambda} E, \tag{A1c}$$

$$\Delta E_{\mathrm{Gr}} = 2.35 \cdot \delta_{\mathrm{Grt}} \cdot \frac{\sin\alpha_0 + \sin\beta_n}{a_0 |n| \lambda} E, \tag{A1d}$$

$$\Delta E_{\mathrm{FM}} = 2.35 \cdot (2\delta_{\mathrm{FMs}}) \cdot \frac{\sin\beta_n \cdot \sin\theta_{\mathrm{FM}}}{a_0 |n| \lambda} E, \tag{A1e}$$

$$\Delta E_{\mathrm{Ex}} = \Sigma_{\mathrm{Ex}} \cdot \frac{\sin\beta_n}{r_2 a_0 |n| \lambda} E, \tag{A1f}$$

where ΔE is the energy bandwidth, E is the X-ray energy, λ is the corresponding wavelength, L is the undulator length, and $\sum_y$, δ_{CMs}, δ_{PMt}, δ_{Grt}, δ_{FMs}, and $\sum_{\mathrm{Ex}}$ represent the RMS electron-beam size (vertical), the RMS sagittal slope error of the M1 collimated mirror, the RMS tangential slope error of the M2 plane mirror, the RMS tangential slope error of the grating, the RMS sagittal slope error of the M3 focus mirror, and the exit slit tangential opening, respectively. r_1 and r_2 represent the lengths of the entrance arm and the exit arm with respect to the grating. a_0 is the constant line density of the grating, and n is the diffraction order. α_0 and β_n are the X-ray grazing incidence angle and diffraction angle of the grating, which are determined by the MLBG structure. θ_{CM} and θ_{FM} are the grazing incidence angles of M1 and M3.

The primary beamline resolution is a quadratic sum of the six contributions:

$$\Delta E_{\mathrm{BL}} = [(\Delta E_S)^2 + (\Delta E_{\mathrm{CM}})^2 + (\Delta E_{\mathrm{PM}})^2 + (\Delta E_{\mathrm{Gr}})^2 + (\Delta E_{\mathrm{FM}})^2 + (\Delta E_{\mathrm{Ex}})^2]^{1/2}. \tag{A2}$$

The values of beamline parameters used to calculate energy resolution are shown in Table 2.

Table 2. Beamline Parameters[a]

	Length of the Undulator (m)	r_1 (m)	r_2 (m)	Σ_y (m)	δ_{PMt} (rad)	δ_{Grt} (rad)	δ_{CMs} (rad)	δ_{FMs} (rad)	Σ_{Ex} (m)	θ_{FM} (deg)	θ_{CM} (deg)
Ultrahigh-resolution design	4.5	30	15	6.4×10^{-6}	1.2×10^{-7}	9×10^{-8}	4.5×10^{-7}	4.5×10^{-7}	1×10^{-5}	0.7	0.7
Reduced-length design	4.5	10	5	6.4×10^{-6}	1.2×10^{-7}	9×10^{-8}	4.5×10^{-7}	4.5×10^{-7}	1×10^{-5}	0.7	0.7

[a]The values primarily refer to Ref. [20].

Table 3. SVLS Grating Parameters and Spectrometer Geometry

Instrument Design Category	Grating Number	Diffraction Order	SVLS Grating Parameter a_0 (l/mm)	a_1 (l/mm^2)	a_2 (l/mm^3)	R (mm)	Spectrometer Geometry at 2.5 keV r_1 (mm)	r_2 (mm)
Ultrahigh-resolution design	SVLSG1	−1st	2400	0.1096	-2.046×10^{-4}	132,361	3000.00	10,801.08
	SVLSG2	−2nd	2400	0.1057	-1.477×10^{-4}	112,825	3000.00	11,628.62
	SVLSG3	−3rd	2400	0.1013	-1.188×10^{-4}	104,038	3000.00	12,257.03
	SVLSG4	−4th	2400	0.1141	-8.704×10^{-5}	110,443	2795.95	12,873.09
	SVLSG8	−8th	2400	0.1492	-3.785×10^{-5}	127,488	1875.70	13,579.45
	SVLSG1-SLG	−1st	2400	0.1617	-8.588×10^{-5}	245,535	2698.34	12,857.90
Reduced-length design	SVLSG8'	−8th	2400	0.4553	-3.524×10^{-4}	41,780	614.69	4450.17

APPENDIX B: ENERGY RESOLUTION OF THE SVLS GRATING SPECTROMETER

Similar to the beamline, the spectrometer's energy resolution is determined by the combined contributions of three main factors: the photon source, the grating, and the detector:

$$\Delta E_S = \Delta_S \frac{\sin \alpha_0}{r_1 a_0 |n| \lambda} E, \tag{B1a}$$

$$\Delta E_{\mathrm{SE}} = \Delta_{\mathrm{SE}} \frac{1}{\tan[(\alpha_0 - \beta_n)/2]} E, \tag{B1b}$$

$$\Delta E_D = \Delta_D \sin \gamma \frac{\sin \beta_n}{r_2 a_0 |n| \lambda} E, \tag{B1c}$$

$$\Delta E = (\Delta E_S^2 + \Delta E_{\mathrm{SE}}^2 + \Delta E_D^2)^{1/2}, \tag{B1d}$$

where ΔE_S, ΔE_{SE}, and ΔE_D represent the energy bandwidth contributions of source size, slope error of the grating, and spatial resolution of detector. ΔE is the total energy bandwidth. Δ_S is the source size, and it is equal to 2 μm. Δ_{SE} is the slope error of the grating, and it is equal to 2×10^{-7} rad (FWHM). Δ_D is the spatial resolution, and it is equal to 2 μm. γ is the detector inclination with respect to the central ray, and it is equal to 20°. The central line density of VLS grating a_0 is 2400 l/mm. α_0 and β_n are determined by the maximum efficiency condition of the MLBG structure. The entrance arm r_1 and the exit arm r_2 of the spectrometer are determined by minimizing the total energy bandwidth [37]:

$$r_1 = \frac{L}{\left(\frac{\Delta_D \sin \gamma \sin \beta_n}{\Delta_S \sin \alpha_0}\right)^{2/3} + 1}, \tag{B2a}$$

$$r_2 = \frac{\sin^2 \beta_n}{\frac{\sin \alpha_0 + \sin \beta_n}{R} - \frac{\sin^2 \alpha_0}{r_1} - a_1 n \lambda}, \tag{B2b}$$

where L is the total spectrometer length, and it is equal to $r_1 + r_2$. R is the grating radius. a_1 is the linear VLS term of the grating.

The radius and VLS coefficients of the grating are optimized at 2.5 keV based on the design method introduced in the analytical section of Ref. [37], assuming a mechanical constraint condition of a typical spectrometer aimed at high resolution [20]. The design results are shown in Table 3.

Funding. National Key Research and Development Program of China (2022YFA1603503); National Natural Science Foundation of China (12075170).

Disclosures. The authors declare no conflicts of interest.

Data Availability. No data were generated or analyzed in the presented research.

REFERENCES

1. M. Hepting, D. Li, C. J. Jia, *et al.*, "Electronic structure of the parent compound of superconducting infinite-layer nickelates," Nat. Mater. **19**, 381–385 (2020).
2. H. Q. Wang, J. Xu, X. Lin, *et al.*, "Determination of the embedded electronic states at nanoscale interface via surface-sensitive photoemission spectroscopy," Light Sci. Appl. **10**, 153 (2021).
3. T. Reuss, S. S. Nair Lalithambika, C. David, *et al.*, "Advancements in liquid jet technology and X-ray spectroscopy for understanding energy conversion materials during operation," Acc. Chem. Res. **56**, 203–214 (2023).
4. F. Wilhelm, J.-P. Sanchez, D. Braithwaite, *et al.*, "Investigating the electronic states of UTe_2 using X-ray spectroscopy," Commun. Phys. **6**, 96 (2023).
5. N. Joudeh and D. Linke, "Nanoparticle classification, physicochemical properties, characterization, and applications: a comprehensive review for biologists," J. Nanobiotechnol. **20**, 262 (2022).
6. M. A. Newton, A. J. Knorpp, V. L. Sushkevich, *et al.*, "Active sites and mechanisms in the direct conversion of methane to methanol using Cu in zeolitic hosts: a critical examination," Chem. Soc. Rev. **49**, 1449–1486 (2020).
7. A. Nag, A. Nocera, S. Agrestini, *et al.*, "Quadrupolar magnetic excitations in an isotropic spin-1 antiferromagnet," Nat. Commun. **13**, 2327 (2022).
8. G. Qian, J. Wang, H. Li, *et al.*, "Structural and chemical evolution in layered oxide cathodes of lithium-ion batteries revealed by synchrotron techniques," Natl. Sci. Rev. **9**, nwab146 (2022).
9. M. Righetto, D. Giovanni, S. S. Lim, *et al.*, "The photophysics of Ruddlesden-Popper perovskites: a tale of energy, charges, and spins," Appl. Phys. Rev. **8**, 011318 (2021).
10. D.-H. Liu, Z. Bai, M. Li, *et al.*, "Developing high safety Li-metal anodes for future high-energy Li-metal batteries: strategies and perspectives," Chem. Soc. Rev. **49**, 5407–5445 (2020).
11. B. M. Tackett, J. H. Lee, and J. G. Chen, "Electrochemical conversion of CO_2 to syngas with palladium-based electrocatalysts," Acc. Chem. Res. **53**, 1535–1544 (2020).

12. R. H. Adnan, J. M. L. Madridejos, A. S. Alotabi, *et al.*, "A review of state of the art in phosphine ligated gold clusters and application in catalysis," Adv. Sci. **9**, 2105692 (2022).
13. G. E. Cutsail Iii and S. DeBeer, "Challenges and opportunities for applications of advanced X-ray spectroscopy in catalysis research," ACS Catal. **12**, 5864–5886 (2022).
14. K. O. Kvashnina and S. M. Butorin, "High-energy resolution X-ray spectroscopy at actinide $M_{4,5}$ and ligand K edges: what we know, what we want to know, and what we can know," Chem. Commun. **58**, 327–342 (2022).
15. P. Northrup, A. Leri, and R. Tappero, "Applications of "tender" energy (1–5 keV) X-ray absorption spectroscopy in life sciences," Protein Peptide Lett. **23**, 300–308 (2016).
16. B. Abraham, S. Nowak, C. Weninger, *et al.*, "A high-throughput energy-dispersive tender X-ray spectrometer for shot-to-shot sulfur measurements," J. Synchrotron Rad. **26**, 629–634 (2019).
17. K. Dardenne, S. Duckworth, X. Gaona, *et al.*, "A combined study of Tc redox speciation in complex aqueous systems: wet-chemistry, Tc K-/L_3-edge X-ray absorption fine structure, and *ab initio* calculations," Inorg. Chem. **60**, 12285–12298 (2021).
18. F. Siewert, B. Löchel, J. Buchheim, *et al.*, "Gratings for synchrotron and FEL beamlines: a project for the manufacture of ultra-precise gratings at Helmholtz Zentrum Berlin," J. Synchrotron Rad. **25**, 91–99 (2018).
19. A. Sokolov, Q. S. Huang, F. Senf, *et al.*, "Optimized highly efficient multilayer-coated blazed gratings for the tender X-ray region," Opt. Express **27**, 16833–16846 (2019).
20. K. J. Zhou, A. Walters, M. Garcia-Fernandez, *et al.*, "I21: an advanced high-resolution resonant inelastic X-ray scattering beamline at diamond light source," J. Synchrotron Radiat. **29**, 563–580 (2022).
21. V. N. Strocov, T. Schmitt, U. Flechsig, *et al.*, "High-resolution soft X-ray beamline ADRESS at the Swiss light source for resonant inelastic X-ray scattering and angle-resolved photoelectron spectroscopies," J. Synchrotron Radiat. **17**, 631–643 (2010).
22. N. B. Brookes, F. Yakhou-Harris, K. Kummer, *et al.*, "The beamline ID32 at the ESRF for soft X-ray high energy resolution resonant inelastic X-ray scattering and polarisation dependent X-ray absorption spectroscopy," Nucl. Instrum. Methods Phys. Res. A **903**, 175–192 (2018).
23. C. H. Lai, H. S. Fung, W. B. Wu, *et al.*, "Highly efficient beamline and spectrometer for inelastic soft X-ray scattering at high resolution," J. Synchrotron Radiat. **21**, 325–332 (2014).
24. I. Jarrige, V. Bisogni, Y. Zhu, *et al.*, "Paving the way to ultra-high-resolution resonant inelastic X-ray scattering with the SIX beamline at NSLS-II," Synchrotron Radiat. News **31**, 7–13 (2018).
25. J. Miyawaki, K. Fujii, T. Imazono, *et al.*, "Design of ultrahigh energy resolution RIXS beamline at NanoTerasu," J. Phys. Conf. Ser. **2380**, 012030 (2022).
26. X. Yang, H. Wang, M. Hand, *et al.*, "Design of a multilayer-based collimated plane-grating monochromator for tender X-ray range," J. Synchrotron Radiat. **24**, 168–174 (2017).
27. Q. S. Huang, I. V. Kozhevnikov, A. Sokolov, *et al.*, "Theoretical analysis and optimization of highly efficient multilayer-coated blazed gratings with high fix-focus constant for the tender X-ray region," Opt. Express **28**, 821–845 (2020).
28. X. W. Yang, I. V. Kozhevnikov, Q. S. Huang, *et al.*, "Unified analytical theory of single-order soft X-ray multilayer gratings," J. Opt. Soc. Am. B **32**, 506–522 (2015).
29. Q. S. Huang, Q. Jia, J. T. Feng, *et al.*, "Realization of wafer-scale nanogratings with sub-50 nm period through vacancy epitaxy," Nat. Commun. **10**, 2437 (2019).
30. D. L. Voronov, S. Park, E. M. Gullikson, *et al.*, "Highly efficient ultra-low blaze angle multilayer grating," Opt. Express **29**, 16676–16685 (2021).
31. D. Vantelon, N. Trcera, D. Roy, *et al.*, "The LUCIA beamline at SOLEIL," J. Synchrotron Radiat. **23**, 635–640 (2016).
32. P. Ohresser, E. Otero, F. Choueikani, *et al.*, "DEIMOS: a beamline dedicated to dichroism measurements in the 350–2500 eV energy range," Rev. Sci. Instrum. **85**, 013106 (2014).
33. S. Werner, P. Guttmann, F. Siewert, *et al.*, "Spectromicroscopy of nanoscale materials in the tender X-ray regime enabled by a high efficient multilayer-based grating monochromator," Small Methods **7**, 2201382 (2023).
34. T. Warwick, Y.-D. Chuang, D. L. Voronov, *et al.*, "A multiplexed high-resolution imaging spectrometer for resonant inelastic soft X-ray scattering spectroscopy," J. Synchrotron Radiat. **21**, 736–743 (2014).
35. D. L. Voronov, T. Warwick, E. M. Gullikson, *et al.*, "Innovative diffraction gratings for high-resolution resonant inelastic soft X-ray scattering spectroscopy," AIP Conf. Proc. **1741**, 040015 (2016).
36. https://www.synopsys.com/photonic-solutions/rsoft-photonic-device-tools/passive-device-diffractmod.html.
37. V. N. Strocov, T. Schmitt, U. Flechsig, *et al.*, "Numerical optimization of spherical variable-line-spacing grating X-ray spectrometers," J. Synchrotron Radiat. **18**, 134–142 (2011).
38. R. Reininger, "The in-focus variable line spacing plane grating monochromator," Nucl. Instrum. Methods Phys. Res. A **649**, 139–143 (2011).
39. X. Yang and T.-C. Weng, "A compact extreme ultraviolet high-throughput spectrometer based on the multilayer varied-line-spacing grating," Rev. Sci. Instrum. **92**, 123104 (2021).
40. D. L. Windt, "IMD—software for modeling the optical properties of multilayer films," Comput. Phys. **12**, 360–370 (1998).
41. I. V. Kozhevnikov, Q. Huang, Y. Zhuang, *et al.*, "Applicability of the Névot-Croce factor in analysis of X-ray reflection from a rough surface," Opt. Commun. **557**, 130318 (2024).
42. J. Dvorak, I. Jarrige, V. Bisogni, *et al.*, "Towards 10 meV resolution: the design of an ultrahigh resolution soft X-ray RIXS spectrometer," Rev. Sci. Instrum. **87**, 115109 (2016).
43. K. J. Kim, "Optical and power characteristics of synchrotron radiation sources," Opt. Eng. **34**, 342–352 (1995).

134.30.220.197 (s 2025-01-31 16:12:15)